TiO$_2$ Nanosheet Arrays with Layered SnS$_2$ and CoO$_x$ Nanoparticles for Efficient Photoelectrochemical Water Splitting

Zhou Cao⬤, Yanling Yin⬤, Peng Fu⬤, Dong Li⬤, Yulan Zhou⬤, Yuanwen Deng⬤, Yuehua Peng⬤, Weike Wang⬤, Weichang Zhou⬤ and Dongsheng Tang*⬤

Abstract

Converting solar energy into sustainable hydrogen fuel by photoelectrochemical (PEC) water splitting is a promising technology to solve increasingly serious global energy supply and environmental issues. However, the PEC performance based on TiO$_2$ nanomaterials is hindered by the limited sunlight-harvesting ability and its high recombination rate of photogenerated charge carriers. In this work, layered SnS$_2$ absorbers and CoO$_x$ nanoparticles decorated two-dimensional (2D) TiO$_2$ nanosheet array photoelectrode have been rationally designed and successfully synthesized, which remarkably enhanced the PEC performance for water splitting. As the result, photoconversion efficiency of TiO$_2$/SnS$_2$/CoO$_x$ and TiO$_2$/SnS$_2$ hybrid photoanodes increases by 3.6 and 2.0 times under simulated sunlight illumination, compared with the bare TiO$_2$ nanosheet arrays photoanode. Furthermore, the TiO$_2$/SnS$_2$/CoO$_x$ photoanode also presented higher PEC stability owing to CoO$_x$ catalyst served as efficient water oxidation catalyst as well as an effective protectant for preventing absorber photocorrosion.

Keywords: TiO$_2$ nanosheet arrays, Tin sulfide, Heterojunction, Photocatalysis, Photoelectrochemical water splitting

Background

Nowadays, with the emergence of non-renewable fossil fuel concerns and environmental pollutions caused by conventional fossil fuel combustion, there is an urgent need to seek a sustainable clean, high photostability, non-toxicity, low cost, and environmental strategy for the generation of clean fuels [1–4]. Photoelectrochemical (PEC) water splitting is well recognized as an ideal alternative to explore attractive sustainable energy sources and technologies since the initial report on PEC water splitting in 1972 [5–7]. Photogenerated electron-hole pairs are spatially separated and transferred and subsequently participates in the water-splitting processes. Titanium dioxide (TiO$_2$) is a promising semiconductor material candidate owing to its intrinsic advantages of high chemical stability, favorable band edge positions, earth-abundant, and nontoxicity [8–11]. However, TiO$_2$,

as a large band-gap semiconductor (ca. 3.2 eV), only absorb the ultraviolet (UV) light. Moreover, its high rate of photoinduced charge carrier recombination and low photoelectric-conversion efficiency limit substantially the practical photocatalytic activity [12–15]. It is highly desirable to construct the efficient geometric nanostructures for improving photoconversion efficiency of PEC water splitting, such as nanowires [16], nanorods [17], nanotubes [18], nanobelts [19], and nanofibers [20]. Recently, different morphological TiO$_2$ materials have been applied to drive water splitting by using sunlight [21–23]. However, the water-splitting efficiency is unsatisfactory owing to the accompaniment of grain boundary effect and deficient specific surface area in these nanostructures. Therefore, two-dimensional (2D) vertically aligned TiO$_2$ nanosheet array structure has attracted intense interest in the PEC water splitting. Compared to other one-dimensional (1D) nanostructures, anatase TiO$_2$ nanosheet arrays with high proportion of exposed {001} facets have been proven to be an active phase when used as a photocatalyst [24–27]. Besides, the vertically grown TiO$_2$ nanosheet arrays

* Correspondence: dstang@hunnu.edu.cn
Synergetic Innovation Center for Quantum Effects and Application, Key Laboratory of Low-dimensional Quantum Structures and Quantum Control of Ministry of Education, School of Physics and Electronics, Hunan Normal University, Changsha 410081, People's Republic of China

Cao *et al. Nanoscale Research Letters* (2019) 14:342

Page 2 of 9

provide an unobstructed transportation pathway for electron transfer to substrates, and the high photocatalytic activity {001} facet-dominated anatase TiO_2 has an extraordinary advantage on the separation of photogenerated charge carriers.

Nevertheless, the practical applications of TiO_2-based water splitting systems are limited because not only the narrow light absorption region resulted from large bandgap, but also its low quantum efficiency and high photogenerated charge carriers recombination rate. Therefore, considerable efforts have been paid to improve the solar light absorption ability and conversion efficiency, for instance, ions doping [28, 29], coupling metal plasmonic nanostructures [30–32], or photosensitization of semiconductors with small bandgap [33–35]. Alternatively, heterogeneous junction constructed with narrow-bandgap photosensitizer has been widely recognized to be an available method to promote efficiently charge carrier separation and extend light absorption ability of the photocatalytic materials [36–39]. Typically, tin (IV) disulfide (SnS_2) with a suitable bandgap energy of 2.4 eV has attracted significant attention for its remarkable optical and electrical properties. As a member of the layered metal chalcogenide semiconductor, 2D SnS_2 nanosheets have been demonstrated as an attractive photocatalyst in PEC solar water splitting because of the effective light absorption ability, short carrier transport distances, and large specific surface area [40–43]. Alternatively, the type II heterojunction combined SnS_2 with TiO_2 has been considered as an efficient route to enhance significantly the light absorption ability as well as improve charge separation efficiency [44, 45]. Furthermore, oxygen evolution, which is the four electrons transfer reaction, is usually considered to be a kinetics controlling step. The water-splitting efficiency can be further enhanced through the integration of cobalt-based catalysts; the catalyst acts as active sites for water oxidation, provides a lower over-potential, and prevents photocorrosion in the water-splitting process [46–48].

In this work, vertically aligned TiO_2 nanosheet arrays were applied in $TiO_2/SnS_2/CoO_x$ heterojunction photoelectrodes for PEC water splitting. CoO_x nanoparticles, which are known to be excellent water oxidation catalysts, were loaded on TiO_2/SnS_2 nanosheet arrays to construct triple hybrid photoanodes. The hybrid semiconducting photoanodes were fabricated by simple hydrothermal or solvothermal process, and the detailed prepared method characterization was discussed subsequently. With CoO_x loading, the performance of TiO_2/SnS_2 photoanode was improved markedly. $TiO_2/SnS_2/CoO_x$ composite nanosheet array photoanode exhibits remarkably improved performances for the PEC water splitting.

Methods

Chemicals and Reagents

Tetrabutyl titanate ($C_{16}H_{36}O_4Ti$, Aladdin Chemistry Co., Ltd., ≥ 99%), ammonium hexafluorotitanate ($(NH_4)_2TiF_6$, Sinopharm Chemical Reagent Co., Ltd., AR), tin (IV) chloride pentahydrate ($SnCl_4·5H_2O$, Sinopharm Chemical Reagent Co., Ltd., ≥ 99%), thioacetamide (CH_3CSNH_2, Sinopharm Chemical Reagent Co., Ltd., ≥ 99%), cobalt (II) acetate tetrahydrate ($Co(CH_3COO)_2·4H_2O$, Sinopharm Chemical Reagent Co., Ltd., ≥ 99.5%), ammonium solution ($NH_3·H_2O$, 25 wt%), concentrated hydrochloric acid (36–38 wt%), acetone (AR), and ethanol (AR) were obtained from Tianjin Chemical Reagents Plant, China. All chemicals were used as received without any further purification.

Preparation of TiO₂ Nanosheet Arrays

TiO_2 nanosheet array photoelectrodes were fabricated onto fluorine-doped tin oxide (FTO)-coated conductive glass substrates using a facile hydrothermal process [49]. In a typical procedure, 10 ml of concentrated hydrochloric acid and 10 ml of deionized (DI) water (18.25 MΩ cm) were mixed under strong stirring at room temperature. Subsequently, 0.4 ml of tetrabutyl titanate was dropped to the mixed solution and stirred vigorously for 5 min to obtain a transparent solution. Next, 0.2 g of ammonium hexafluorotitanate ($(NH_4)_2TiF_6$) was added and further stirred for 10 min. The as-prepared mixture precursor solution was transferred to a Teflon-lined autoclave (100 ml in volume). The FTO substrates (14 Ω/square) were ultrasonically cleaned with acetone, ethanol, and DI water in sequence and dried prior to the experiment. Then, the conductive FTO substrate was placed facing down into the autoclave obliquely. The autoclave was conducted at 170 °C for 10 h and then naturally cooled down. After the synthesis, the sample was washed with DI water and air-dried at room temperature. To increase the crystallinity of TiO_2 nanosheet arrays, the as-prepared samples were annealed in air atmosphere at 550 °C for 3 h.

Fabrication of TiO₂/SnS₂ Hybrid

The hybrid TiO_2/SnS_2 nanosheet arrays can be fabricated as described in the following preparation details; 2D SnS_2 were grown on TiO_2 nanosheet arrays by low-temperature solvothermal method. A mixture solution containing 10 ml absolute ethanol, 10 mM $SnCl_4$, and 30 mM thioacetamide was magnetically stirred and prepared in the solvothermal process. Then FTO substrates covered with TiO_2 nanosheet arrays were vertically inserted into the precursor solution. During the deposition, the temperature was heated at 80 °C for 1 h. After cooling down, the fabricated samples were rinsed by

Cao *et al. Nanoscale Research Letters*   (2019) 14:342

Page 3 of 9

absolute ethanol and DI water several times and annealed in Ar atmosphere at 250 °C for 2 h.

Synthesis of $TiO_2/SnS_2/CoO_x$ Photoelectrodes

Finally, CoO_x nanoparticles were loaded on TiO_2/SnS_2 nanosheet arrays by a modified solvothermal method reported previously [50, 51]. In detail, 0.25 ml ammonium solution was dropwise added into 18 ml ethanol solution containing 5 mM cobalt acetate under vigorous stirring. Subsequently, the as-prepared solution was transferred into a 25-ml autoclave and two pieces of TiO_2/SnS_2 electrodes were obliquely placed into the bottom of the autoclave. Next, the autoclave was heated and kept at 120 °C for 1 h. After the solvothermal process finished, the obtained $TiO_2/SnS_2/CoO_x$ photoelectrodes were thoroughly rinsed with DI water and dried in air.

Characterization

X-ray diffraction (XRD) patterns were obtained using a Bruker D8 Discover X-ray diffractometer with Cu Kα radiation ($\lambda = 0.15406$ nm). Scanning electron microscopic images were obtained using a FEI NovaSEM-450 field emission scanning electron microscope (SEM) equipped with an Oxford X-max20 energy dispersive X-ray spectrometer (EDS). The optical absorption spectra were recorded on a Perkin Elmer Lambda 750 coupled with a 60-mm integrating sphere attachment. Transmission electron microscopy (TEM) images were recorded in a FEI Tecnai F20 transmission electron microscope with operating voltage 200 kV. Raman spectra were recorded on a LabRAM HR Evolution Horiba JY high-resolution Raman spectrometer with a wavelength of 633 nm as the excitation source. X-ray photoelectron spectroscopy (XPS) was recorded by a Thermo Fisher Scientific-Escalab 250Xi X-ray photoelectron spectrometer with a monochromatic Al Ka irradiation.
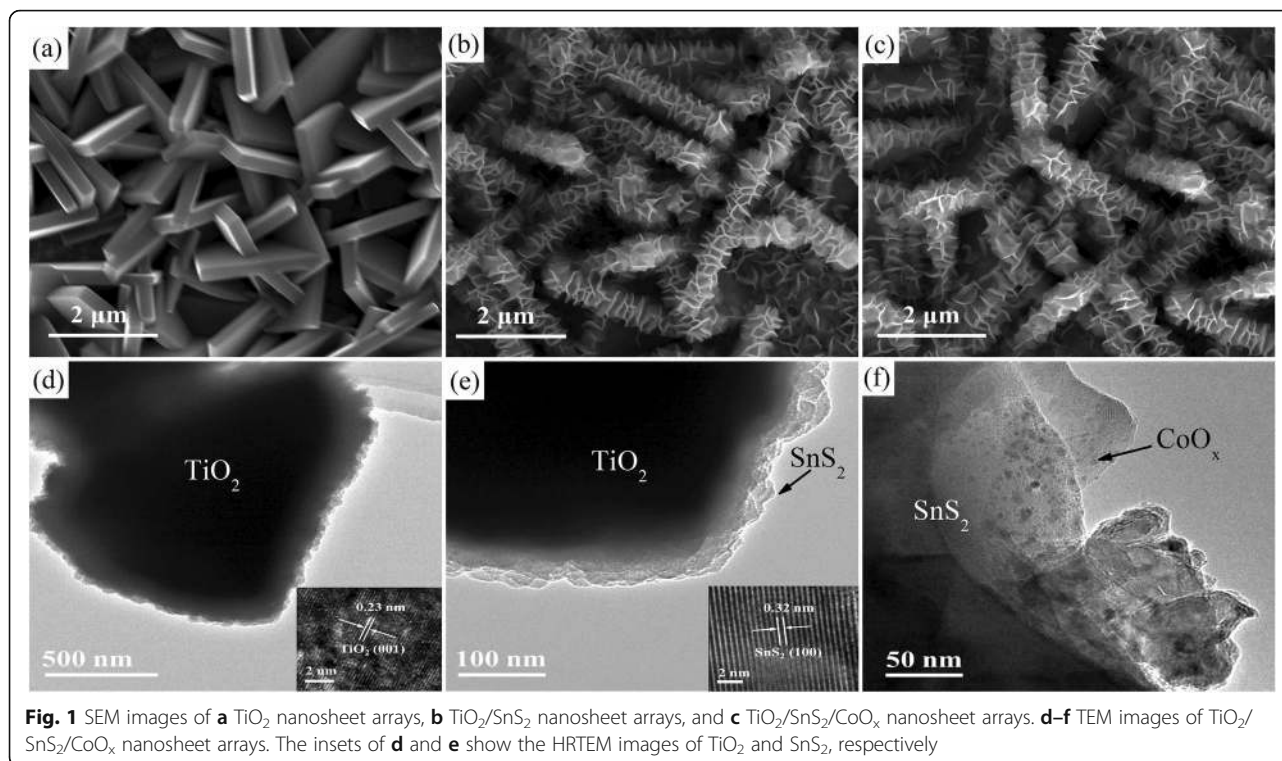
PEC Measurements

PEC measurements were carried out using a standard three-electrode cell with the fabricated electrode used as a working electrode, a Pt wire used as a counter electrode, and Ag/AgCl used as reference electrode at an electrochemical workstation (CorrTest, CS350). All PEC measurements were performed with the effective surface area of the working electrode kept as 2 cm^2 and illuminated from the front side in 0.5 M Na$_2$SO$_4$ (pH = 6.8) electrolyte. The electrode potential of the working electrodes (vs. Ag/AgCl) can be converted to the reversible hydrogen electrode (RHE) potential by the Nernst equation: $E_{RHE} = E_{Ag/AgCl} + 0.059 \text{ pH} + E^{\theta}_{Ag/AgCl}$, where E_{RHE} is the converted potential vs. RHE, $E^{\theta}_{Ag/AgCl}$ is 0.1976 V at 25 °C, and $E_{Ag/AgCl}$ is the applied potential against the Ag/AgCl reference electrode. The photocurrent density-

potential (i-v) measurements were carried out at a scan rate of 10 mV/s under the solar simulator (7IS0503A) using a 150 W xenon lamp equipped with an AM 1.5G filter as illumination source (100 mW/cm^2). The amperometric photocurrent-time (i-t) curves were evaluated with light irradiation on/off cycles under an applied potential of 1.23 V vs. RHE. Electrochemical impedance spectroscopy (EIS) was carried out in the frequency range of 0.01–100 kHz and an AC voltage amplitude of 5 mV at an open-circuit potential.

Results and Discussion

The process for fabrication of the $TiO_2/SnS_2/CoO_x$ nanosheet array photoanode is illustrated (Additional file 1: Scheme S1). The morphology and structure images of the pristine TiO_2 and hybrid nanosheet array photoelectrodes are displayed in Fig. 1 by SEM and TEM observation. In order to ensure that each photoelectrode has an equal density of nanosheet arrays, the pristine TiO_2 nanosheet array photoelectrode was prepared in one-pot hydrothermal synthesis. Obviously, the surface of FTO substrate is uniformly covered with smooth TiO_2 nanosheet arrays and the thickness of nanosheet is typically about 280 nm as observed from Fig. 1a. In addition, the cross-section image shows that the film is composed of vertically aligned TiO_2 nanosheet arrays and the height of nanosheet arrays is about 1 μm (Additional file 1: Figure S1). It is apparent that the entire surfaces of TiO_2 nanosheet arrays become rough after the deposition of SnS_2 layer (Fig. 1b). With the loading of CoO_x nanoparticles, the SEM picture of the nanosheet arrays has almost no significant difference owing to CoO_x nanoparticle high dispersion and low concentration, as shown in Fig. 1c. However, EDS reflect the presence of CoO_x nanoparticles on the surface of hybrid (Additional file 1: Figure S2). As revealed by Fig. 1d, HRTEM images further reveal that the nanosheets have a single-crystalline structure, which clearly shows the lattice fringes of 0.23 nm, corresponding to the *d*-spacing values of the anatase TiO_2 (001) planes. In the TEM image in Fig. 1e of an individual TiO_2/SnS_2 heterojunction nanosheet, it clearly illustrates that the TiO_2 nanosheets are covered by the SnS_2 outlayer. As can be seen in the HRTEM images, the lattice *d*-spacing is 0.32 nm, corresponding to (100) fringe plane of hexagonal SnS_2. As seen in Fig. 1f, the HRTEM image shows that CoO_x nanoparticles are evenly dispersed on the surface of TiO_2/SnS_2 nanosheet arrays.

XRD measurement was used to identify the crystallinity and crystal structure of hybrid photoelectrodes. As described in Fig. 2a, all of the diffraction peaks are readily indexed to the typical anatase TiO_2 (JCPDS 21-1272) and hexagonal SnS_2 (JCPDS 21-1231) apart from the FTO substrate peaks, which revealed the coexistence of

Cao *et al. Nanoscale Research Letters*   (2019) 14:342

Page 4 of 9

Fig. 1 SEM images of **a** TiO$_2$ nanosheet arrays, **b** TiO$_2$/SnS$_2$ nanosheet arrays, and **c** TiO$_2$/SnS$_2$/CoO$_x$ nanosheet arrays. **d–f** TEM images of TiO$_2$/SnS$_2$/CoO$_x$ nanosheet arrays. The insets of **d** and **e** show the HRTEM images of TiO$_2$ and SnS$_2$, respectively

TiO$_2$ and SnS$_2$ in the hybrid electrodes. However, diffraction peaks corresponding to CoO$_x$ (CoO or Co$_3$O$_4$) were not evidently detected, probably because of their low concentration and high dispersion on the hybrid electrode surface. To further verify the crystalline phase of hybrid photoelectrodes, an additional Raman spectrum was performed (Additional file 1: Figure S3). The Raman spectrum for the TiO$_2$ nanosheet arrays shows characteristic bands at around 144, 394, 514, and

637 cm^{-1}, corresponding to the Raman active modes in anatase TiO$_2$ with the O–Ti–O vibration of E_g, B_{1g}, A_{1g}, and E_g, respectively [52–54]. The same Raman scattering peaks are observed for the TiO$_2$/SnS$_2$ sample. After the formation of TiO$_2$/SnS$_2$ heterojunction, the A_{1g} mode Raman peak of hexagonal SnS$_2$ at 314 cm^{-1} is observed, verifying the successful introduction of SnS$_2$ layers in the hybrid electrode [55, 56]. The optical absorption spectra of bare TiO$_2$, TiO$_2$/SnS$_2$, and TiO$_2$/SnS$_2$/CoO$_x$

Fig. 2 a XRD pattern and **b** absorption spectra of pristine TiO$_2$, TiO$_2$/SnS$_2$ and TiO$_2$/SnS$_2$/CoO$_x$ nanosheet arrays
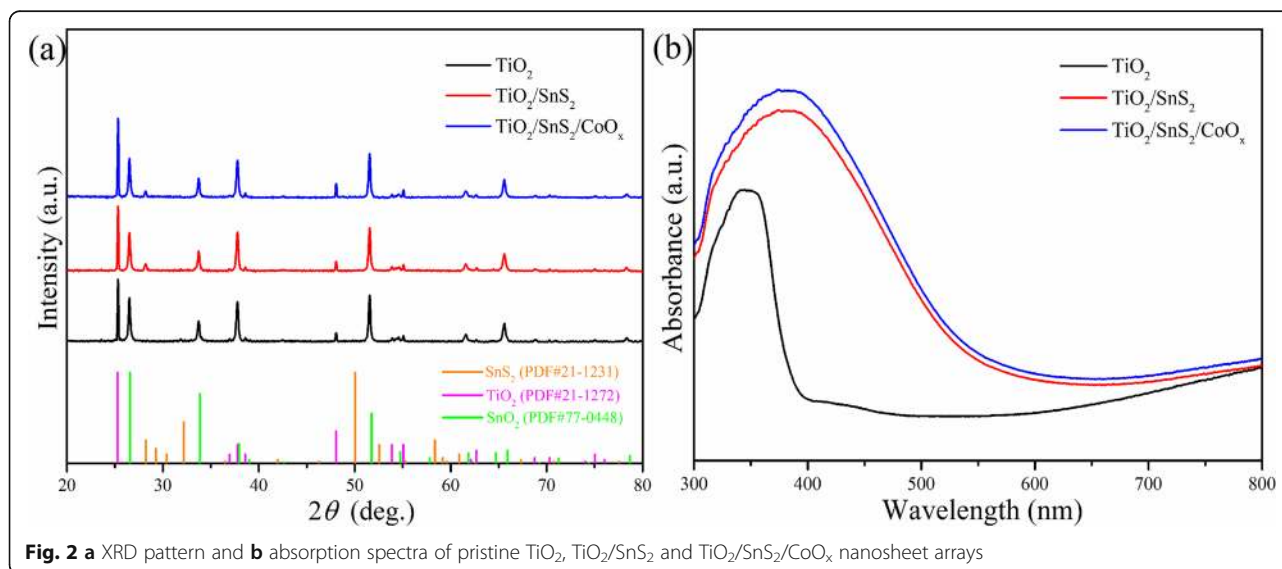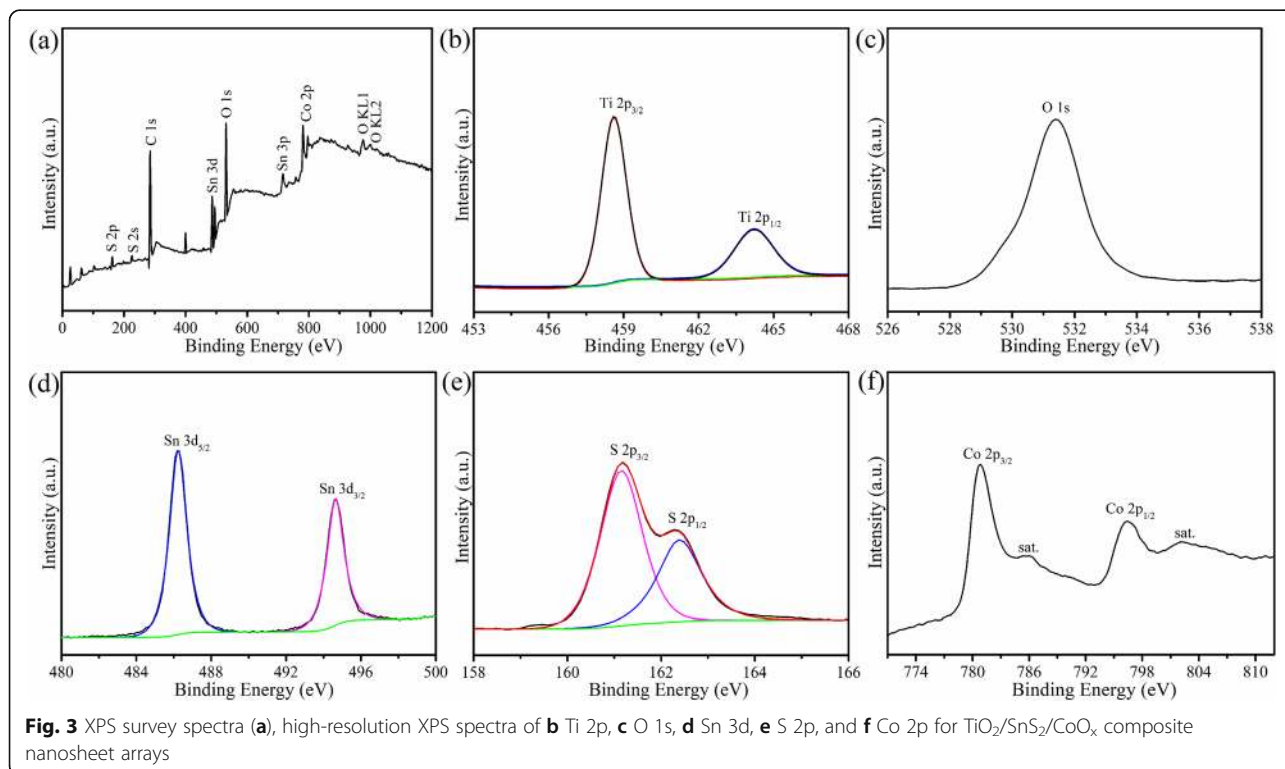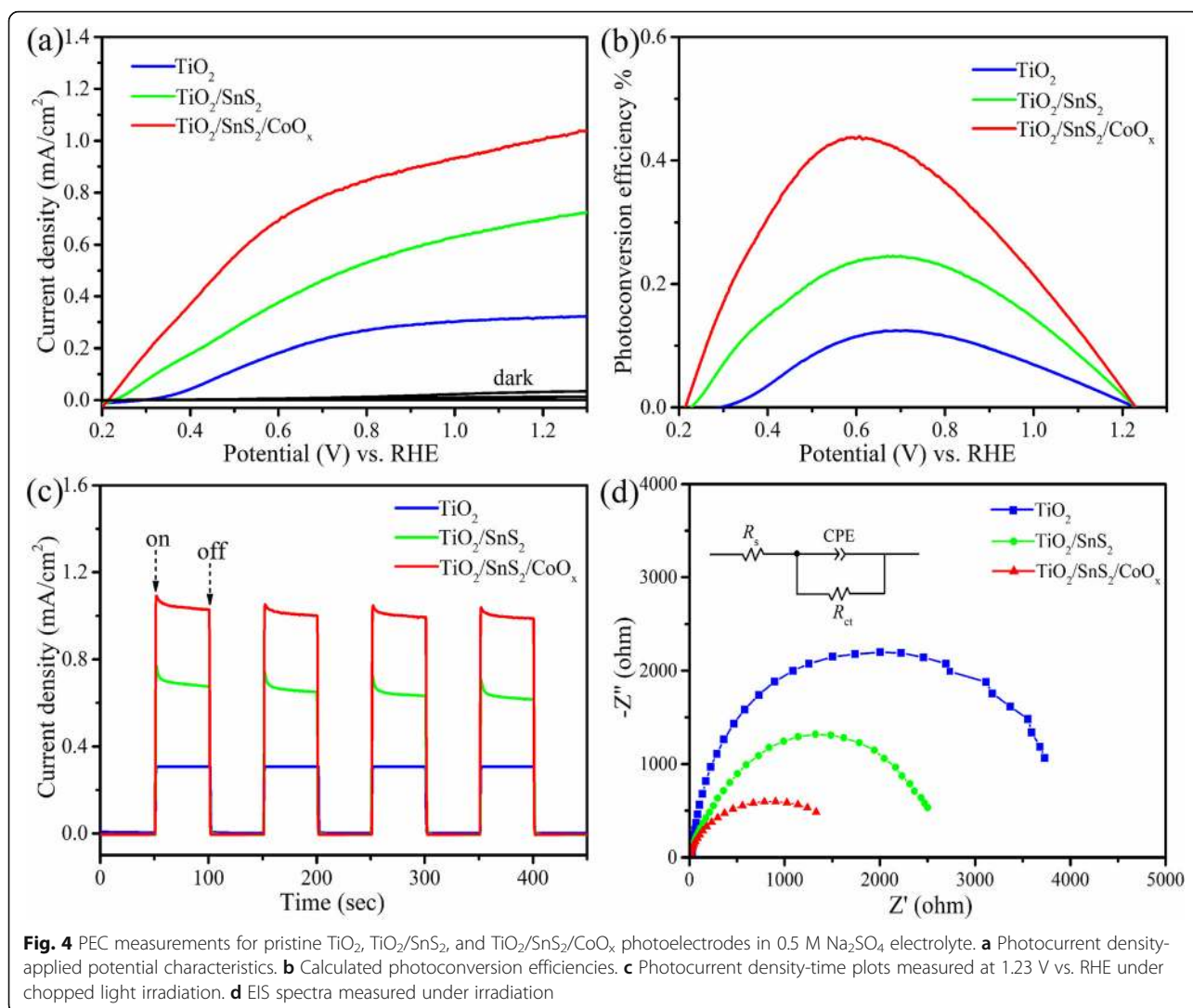
nanosheet arrays are presented in Fig. 2b. The pristine TiO_2 nanosheet array sample shows the characteristic absorption band located at 380 nm, while the TiO_2/SnS_2 hybrid appears a wide visible light absorption edge, which was attributed to the excellent light absorption ability of SnS_2 layer. The corresponding optical energy gap can be subsequently calculated using the following equation: $\alpha h\nu = A(h\nu - E_g)^n$, where α, A, $h\nu$, and E_g are the optical absorption coefficient, a constant, incident photon energy, and the bandgap, respectively. In addition, n is equal to 1/2 for direct bandgap semiconductors while n is equal to 2 for indirect bandgap semiconductors. The energy gap for the bare TiO_2 and pristine SnS_2 was estimated to be 3.2 and 2.4 eV (Additional file 1: Figure S4), respectively [57–60]. After decorating with CoO_x, the absorption spectra of $TiO_2/SnS_2/CoO_x$ nanosheet arrays display similar light absorption bands (ca. 560 nm) to TiO_2/SnS_2 hybrid, which implies absent additional bandgap transition resulted from the introduction of CoO_x catalysts.

To further investigate the valence state and chemical environment, XPS characterization of all the photoelectrodes was measured. As illustrated in Fig. 3a, XPS survey spectrum of the $TiO_2/SnS_2/CoO_x$ hybrid proves the presence of Ti, O, Sn, S, and Co elements. Figure 3b shows the high-resolution XPS spectrum of Ti 2p. The two peaks located at 458.6 and 464.2 eV are ascribed to Ti $2p_{3/2}$ and Ti $2p_{1/2}$, respectively, indicating the presence of Ti^{4+} species. Figure 3c shows the binding energy

of the O 1s core level around 531.4 eV, which is corresponding to the lattice oxygen atoms of Ti–O–Ti bond. Two symmetric peaks at the binding energy of 486.47 (Sn $3d_{5/2}$) and 494.88 eV (Sn $3d_{3/2}$) are shown in Fig. 3d, which confirmed the existence of Sn^{4+} in the hybrid electrodes. Meanwhile, the peaks located at 161.2 and 162.3 eV are corresponding to S $2p_{3/2}$ and S $2p_{1/2}$ states (Fig. 3e), demonstrating the formation of the SnS_2 outlayer. Furthermore, two distinct peaks located at 796.5 (Co $2p_{1/2}$) and 780.6 eV (Co $2p_{3/2}$) with the satellite peaks are presented in Fig. 3f, which is ascribed to the coordination of both the Co^{3+} and Co^{2+}. That is a demonstration, in fact, that the water oxidation catalyst CoO_x (CoO and Co_3O_4) is definitely assembled on the surface of hybrid photoelectrodes. In addition, the atomic percentage of Co element was estimated to be about 4.3 at% based on XPS analysis in the $TiO_2/SnS_2/CoO_x$ nanosheet arrays. As a result, the diffraction peak performed on the previous XRD measurement is not detected because of the low concentration of CoO_x nanoparticles in the hybrid photoelectrodes.

To investigate the PEC performance of these photoelectrodes, the nanosheet arrays were fabricated into the working electrode in a standard three-electrode electrochemical system. Linear sweep voltammetry (LSV) curves of the pristine TiO_2, TiO_2/SnS_2, and $TiO_2/SnS_2/CoO_x$ nanosheet array photoelectrodes are shown in Fig. 4a, in an applied potential range of 0.2 to 1.3 V vs. RHE. Obviously, dark scan LSV curves show an almost
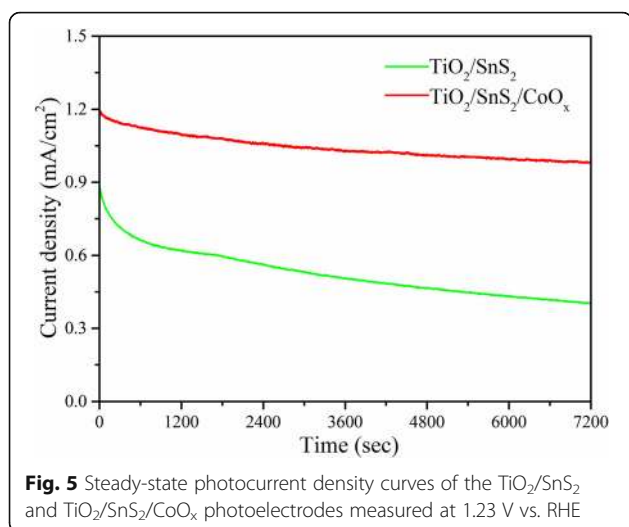

Fig. 3 XPS survey spectra (**a**), high-resolution XPS spectra of **b** Ti 2p, **c** O 1s, **d** Sn 3d, **e** S 2p, and **f** Co 2p for $TiO_2/SnS_2/CoO_x$ composite nanosheet arrays

Fig. 4 PEC measurements for pristine TiO_2, TiO_2/SnS_2, and $TiO_2/SnS_2/CoO_x$ photoelectrodes in 0.5 M Na_2SO_4 electrolyte. **a** Photocurrent density-applied potential characteristics. **b** Calculated photoconversion efficiencies. **c** Photocurrent density-time plots measured at 1.23 V vs. RHE under chopped light irradiation. **d** EIS spectra measured under irradiation

negligible current density for all samples. Nevertheless, the photocurrent of TiO_2 electrode is remarkably enhanced after coated with SnS_2 photosensitizer and then further improved when deposited CoO_x catalysts under simulated sunlight illumination. Furthermore, the onset potential of photocurrent for TiO_2 nanosheet arrays is negatively shifted for TiO_2/SnS_2 and $TiO_2/SnS_2/CoO_x$ nanosheet array electrodes, due to the negative shift of Fermi level and low carrier recombination rate by SnS_2 outlayer and CoO_x catalysts. In addition, the photoconversion efficiency (η) of pristine TiO_2 and TiO_2/SnS_2 and $TiO_2/SnS_2/CoO_x$ photoelectrodes are calculated using the following equation:

$$\eta = I \left(E_{rev}^{\theta} - V \right) / J_{light}$$

where I is the photocurrent density (mA/cm^2), $E\theta$ rev is 1.23 V vs. RHE for the water splitting, V is the measured potential vs. RHE, and J_{light} is the irradiance intensity of

incident light (100 mW/cm^2). Figure 4b displays the photoconversion efficiency plots with applied potential from 0.2 to 1.3 V vs. RHE under light radiation. The pristine TiO_2 photoelectrode displays the optimal photoconversion efficiency of 0.12% at 0.70 V vs. RHE. Remarkably, $TiO_2/SnS_2/CoO_x$ and TiO_2/SnS_2 nanosheet array photoelectrodes exhibit the highest efficiency of 0.44% and 0.24%, about 3.6 and 2.0 times higher compared with pristine TiO_2 nanosheet arrays, respectively. The chopped light photoresponse (*i-t*) curves of the photoanodes measured at 1.23 V vs. RHE, as shown in Fig. 4c. The fast rise-fall changing of the photocurrent density indicates that the charge transport in the photoelectrodes is very quick. In contrast, $TiO_2/SnS_2/CoO_x$ photoelectrode exhibits a higher photocurrent density of 1.05 mA/cm^2, 3.38-fold enhancement compared to bare TiO_2 nanosheet arrays at the same applied bias potential. This is mainly due to the fact that SnS_2 outlayer and CoO_x catalysts would effectively extend the optical

Cao *et al. Nanoscale Research Letters*   (2019) 14:342

Page 7 of 9

Fig. 5 Steady-state photocurrent density curves of the TiO_2/SnS_2 and $TiO_2/SnS_2/CoO_x$ photoelectrodes measured at 1.23 V vs. RHE
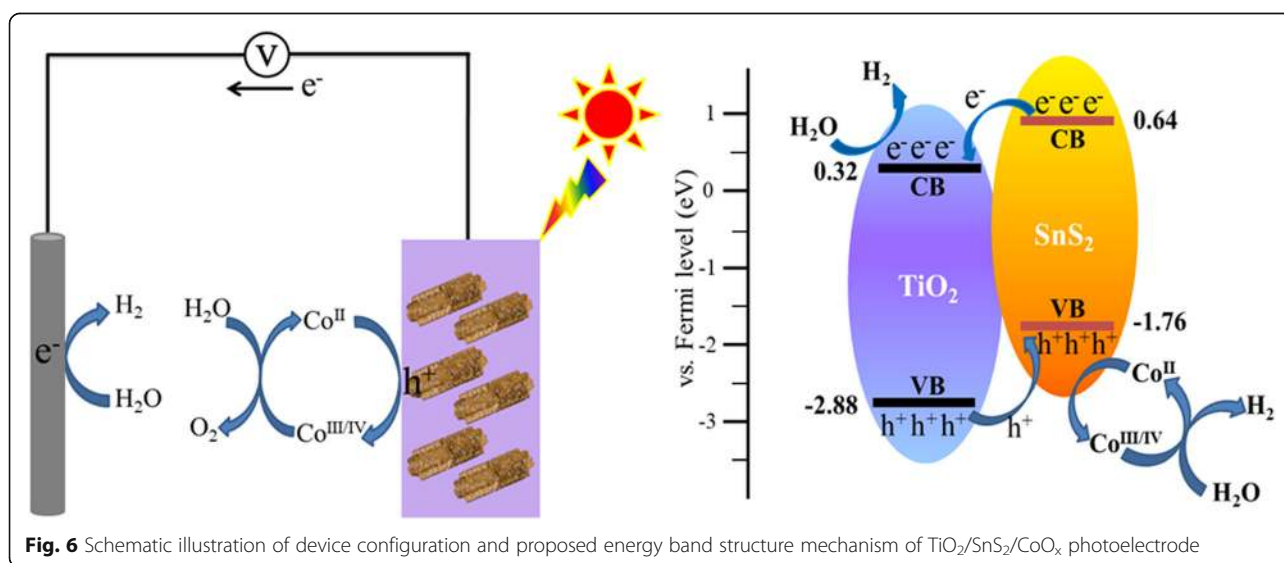
absorption range, accelerate the effective transfer of charge carriers and reduce the charge carrier recombination, thus enhanced photocurrent density. In order to further study the interface charge transport process of photoanodes, electrochemical impedance spectrum (EIS) investigations of the TiO_2, TiO_2/SnS_2, and $TiO_2/SnS_2/CoO_x$ nanosheet arrays are shown in Fig. 4d, measured at open circuit potential under light illumination (100 mW/cm^2). Here, R_s denotes the contact resistances of the electrochemical device, CPE denotes the capacitance phase element, and R_{ct} denotes the interfacial charge transfer resistance. The values of R_{ct} are calculated to be 3780, 2460, and 1650 Ω for TiO_2, TiO_2/SnS_2, and $TiO_2/SnS_2/CoO_x$ nanosheet array electrodes, respectively. Clearly, a smaller arc radius was observed for $TiO_2/SnS_2/CoO_x$ as compared to those of TiO_2 and TiO_2/SnS_2 hybrid photoelectrodes. It is noteworthy that the

reduction of Nyquist arc radius reflects that an effective separation and fast charge transfer of photoinduced charge carriers have occurred at the hetero-junction interface. These results significantly indicate that the introduction of SnS_2 and CoO_x obviously improve the TiO_2 PEC properties.

On the other hand, the photocurrent stability is also very important to further confirm the PEC performance of water splitting. In order to show the photostability of these photoelectrodes, the long-term stability photostability measurements for TiO_2/SnS_2 and $TiO_2/SnS_2/CoO_x$ nanosheet arrays were carried out for 2 h under the continuous simulated sunlight illumination. As presented in Fig. 5, the decrease in photocurrent density of TiO_2/SnS_2 and $TiO_2/SnS_2/CoO_x$ nanosheet array photoanode is about 54.0% and 18.3% in the following measurement period, respectively. The achieved good stability indicates that the photocorrosion process was restrained after the decoration of CoO_x catalysts, and $TiO_2/SnS_2/CoO_x$ nanosheet arrays still retain the primitive structure under simulated sunlight illumination after long-term PEC water splitting process.

Based on the above results, a possible charge transfer mechanism for the hybrid $TiO_2/SnS_2/CoO_x$ nanosheet array photoelectrode is proposed in Fig. 6. When the hybrid heterojunction is irradiated by sunlight, as a narrow photosensitizer with excellently high absorption, SnS_2 is readily excited to generate photoinduced charge carriers under illumination. Eventually, photoinduced electrons on the conduction band (CB) of SnS_2 can be efficiently transferred to the CB of TiO_2 nanosheets by the use of the type-II band alignment (Additional file 1: Figure S5), subsequently transmitted to counter electrode through the extra circuit to drive water splitting reactions. Simultaneously, photogenerated holes are transported to the opposite direction from the valence band (VB) of TiO_2

Fig. 6 Schematic illustration of device configuration and proposed energy band structure mechanism of $TiO_2/SnS_2/CoO_x$ photoelectrode

Cao *et al. Nanoscale Research Letters* (2019) 14:342

Page 8 of 9

to VB of SnS_2 and finally, the photogenerated holes are consumed on the surface of photoanode by photooxidation water process. Furthermore, CoO_x nanoparticles couple effectively to the surface layer of hybrid photoanode, which led to the greatly improved photoconversion efficiency under simulated sunlight irradiation. This suggests that CoO_x nanoparticles further accelerate photooxidation kinetics, reduce significantly the recombination of photogenerated charge carriers, and restrain photocorrosion of the photoanode, which result in increased PEC performance for water splitting.

Conclusions

In summary, we have successfully fabricated a novel 2D architecture heterojunction $TiO_2/SnS_2/CoO_x$ photoanode for PEC water splitting. This ternary hybrid $TiO_2/SnS_2/CoO_x$ photoanode exhibits significantly enhanced photocurrent density. The photoconversion efficiency of $TiO_2/SnS_2/CoO_x$ is about 1.8 and 3.6 times higher than that of the TiO_2/SnS_2 and pristine TiO_2 photoelectrodes, respectively. The enhanced PEC performance can be attributable to improve light absorption ability and reduce photo-generated carrier recombination as a result of the type-II heterojunction constructed between TiO_2 nanosheet and layered SnS_2. Furthermore, CoO_x catalysts further accelerate surface water oxidation kinetics, promote efficient charge separation, and improve PEC stability. This work provides new insight and potential construct of efficient PEC practical applications toward sustainable solar-driven water splitting systems.

Supplementary information

Supplementary information accompanies this paper at https://doi.org/10.1186/s11671-019-3168-7.

Additional file 1: Scheme S1. A schematic illustration of the formation process for the $TiO_2/SnS_2/CoO_x$ nanosheet arrays on FTO substrates. **Figure S1.** Cross-sectional SEM images of (a) pristine TiO_2, (b) TiO_2/SnS_2 and (c) $TiO_2/SnS_2/CoO_x$ nanosheet arrays on FTO substrates, respectively. **Figure S2.** EDS pattern of the $TiO_2/SnS_2/CoO_x$ nanosheet arrays. **Figure S3.** Raman spectra of pristine TiO_2 and TiO_2/SnS_2 nanosheet arrays. **Figure S4.** Optical bandgap of (a) bare TiO_2 nanosheet arrays and (b) pristine SnS_2 samples calculated from the Kubelka-Munk equation. **Figure S5.** (a) UPS spectra of SnS_2 and (b) XPS valence band spectra of the TiO_2/SnS_2 photoelectrode. (DOCX 23095 kb)

Abbreviations

CB: Conduction band; EDS: Energy dispersive X-ray spectrometer; EIS: Electrochemical impedance spectroscopy; FTO: Fluorine-doped tin oxide; LSV: Linear sweep voltammetry; PEC: Photoelectrochemical; RHE: Reversible hydrogen electrode; SEM: Scanning electron microscope; SnS_2: Tin disulfide; TEM: Transmission electron microscopy; TiO_2: Titanium dioxide; VB: Valence band; XPS: X-ray photoelectron spectroscopy; XRD: X-ray diffraction

Authors' Contributions

ZC designed this study and wrote the manuscript. YLY and PF are responsible for the data analysis. DL, YLZ, and YWD contributed to figure modifying and language checking. YHP, WKW, and WCZ helped draft the manuscript. DST supervised the work. All authors read and approved the final manuscript.

References

1. Ma Y, Wang X, Jia Y, Chen X, Han H, Li C (2014) Titanium dioxide-based nanomaterials for photocatalytic fuel generations. Chem Rev 114:9987–10043
2. Yao T, An X, Han H, Chen JQ, Li C (2018) Photoelectrocatalytic materials for solar water splitting. Adv Energy Mater 8:1800210
3. Ge M, Cao C, Huang J, Li S, Chen Z, Zhang K-Q, Al-Deyab SS, Lai Y (2016) A review of one-dimensional TiO_2 nanostructured materials for environmental and energy applications. J Mater Chem A 4:6772–6801
4. Li Y, Wang L, Liang J, Gao F, Yin K, Dai P (2017) Hierarchical heterostructure of $ZnO@TiO_2$ hollow spheres for highly efficient photocatalytic hydrogen evolution. Nanoscale Res Lett 12:531
5. Fujishima A, Honda K (1972) Electrochemical photolysis of water at a semiconductor electrode. Nature 238:37–38
6. Schneider J, Matsuoka M, Takeuchi M, Zhang J, Horiuchi Y, Anpo M, Bahnemann DW (2014) Understanding TiO_2 photocatalysis: mechanisms and materials. Chem Rev 114:9919–9986
7. Cao Z, Yin Y, Yang W, Zhao G, Liu Y, Zhou Y, Peng Y, Wang W, Zhou W, Tang D (2019) Amorphous Co-Pi anchored on $CdSe/TiO_2$ nanowire arrays for efficient photoelectrochemical hydrogen production. J Mater Sci 54:3284–3293
8. Zhong D, Jiang Q, Huang B, Zhang W-H, Li C (2015) Synthesis and characterization of anatase TiO_2 nanosheet arrays on FTO substrate. J Energy Chem 24:626–631
9. Yuan Y-J, Ye Z-J, Lu H-W, Hu B, Li Y-H, Chen D-Q, Zhong J-S, Yu Z-T, Zou Z-G (2015) Constructing anatase TiO_2 nanosheets with exposed (001) facets/layered MoS_2 two-dimensional nanojunctions for enhanced solar hydrogen generation. ACS Catal 6:532–541
10. Gao C, Wei T, Zhang Y, Song X, Huan Y, Liu H, Zhao M, Yu J, Chen X (2019) A photoresponsive rutile TiO_2 heterojunction with enhanced electron-hole separation for high-performance hydrogen evolution. Adv Mater 31:1806596
11. Liu C, Wang L, Tang Y, Luo S, Liu Y, Zhang S, Zeng Y, Xu Y (2015) Vertical single or few-layer MoS_2 nanosheets rooting into TiO_2 nanofibers for highly efficient photocatalytic hydrogen production. Appl Catal B Environ 164:1–9
12. Yu J, Qi L, Jaroniec M (2010) Hydrogen production by photocatalytic water splitting over Pt/TiO_2 nanosheets with exposed (001) facets. J Phys Chem C 114:13118–13125
13. Yang HG, Liu G, Qiao SZ, Sun CH, Jin YG, Smith SC, Zou J, Cheng HM, Lu GQ (2009) Solvothermal synthesis and photoreactivity of anatase TiO_2 nanosheets with dominant {001} facets. J Am Chem Soc 131:4078–4083
14. Yang Y, Liu G, Irvine JT, Cheng HM (2016) Enhanced photocatalytic H_2 production in core-shell engineered rutile TiO_2. Adv Mater 28:5850–5856
15. Wang L, Li Y, Liu Y (2017) Reduced graphene $oxide@TiO_2$ $nanorod@reduced$ graphene oxide hybrid nanostructures for photoelectrochemical hydrogen production. Micro Nano Lett 12:494–496
16. Liao J-Y, Lei B-X, Chen H-Y, Kuang D-B, Su C-Y (2012) Oriented hierarchical single crystalline anatase TiO_2 nanowire arrays on Ti-foil substrate for efficient flexible dye-sensitized solar cells. Energy Environ Sci 5:5750–5757
17. Liu B, Aydil ES (2009) Growth of oriented single-crystalline rutile TiO_2 nanorods on transparent conducting substrates for dye-sensitized solar cells. J Am Chem Soc 131:3985–3990
18. Bavykin DV, Parmon VN, Lapkin AA, Walsh FC (2004) The effect of hydrothermal conditions on the mesoporous structure of TiO_2 nanotubes. J Mater Chem 14:3370–3377

19. Sarkar D, Chattopadhyay KK (2014) Branch density-controlled synthesis of hierarchical TiO_2 nanobelt and tunable three-step electron transfer for enhanced photocatalytic property. ACS Appl Mater Inter 6:10044–10059

20. Zhang Z, Shao C, Li X, Sun Y, Zhang M, Mu J, Zhang P, Guo Z, Liu Y (2013) Hierarchical assembly of ultrathin hexagonal SnS_2 nanosheets onto electrospun TiO_2 nanofibers: enhanced photocatalytic activity based on photoinduced interfacial charge transfer. Nanoscale 5:606–618

21. Chen HM, Chen CK, Liu RS, Zhang L, Zhang J, Wilkinson DP (2012) Nano-architecture and material designs for water splitting photoelectrodes. Chem Soc Rev 41:5654–5671

22. Liu T, Wang J, Liu L, Feng S, Su P, Yang H, Fu W (2018) Enhanced photoelectric performance of CdS/CdSe co-sensitized TiO_2 nanosheets array film. Sustainable Energy Fuels 2:1262–1268

23. Wang L, Duan X, Wang G, Liu C, Luo S, Zhang S, Zeng Y, Xu Y, Liu Y, Duan X (2016) Omnidirectional enhancement of photocatalytic hydrogen evolution over hierarchical "cauline leaf" nanoarchitectures. Appl Catal B Environ 186:88–96

24. Liu S, Yu J, Jaroniec M (2011) Anatase TiO_2 with dominant high-energy {001} facets: synthesis, properties, and applications. Chem Mater 23:4085–4093

25. Xiang Q, Yu J, Wang W, Jaroniec M (2011) Nitrogen self-doped nanosized TiO_2 sheets with exposed {001} facets for enhanced visible-light photocatalytic activity. Chem Commun 47:6906–6908

26. Sajan CP, Wageh S, Al-Ghamdi AA, Yu J, Cao S (2015) TiO_2 nanosheets with exposed {001} facets for photocatalytic applications. Nano Res 9:3–27

27. Han X, Kuang Q, Jin M, Xie Z, Zheng L (2009) Synthesis of titania nanosheets with a high percentage of exposed (001) facets and related photocatalytic properties. J Am Chem Soc 131:3152–3153

28. Li D, Jia J, Zheng T, Cheng X, Yu X (2016) Construction and characterization of visible light active Pd nano-crystallite decorated and C-N-S-co-doped TiO2 nanosheet array photoelectrode for enhanced photocatalytic degradation of acetylsalicylic acid. Appl Catal B Environ 188:259–271

29. Banerjee B, Amoli V, Maurya A, Sinha AK, Bhaumik A (2015) Green synthesis of Pt-doped TiO_2 nanocrystals with exposed (001) facets and mesoscopic void space for photo-splitting of water under solar irradiation. Nanoscale 7:10504–10512

30. Aslam U, Rao VG, Chavez S, Linic S (2018) Catalytic conversion of solar to chemical energy on plasmonic metal nanostructures. Nat Catal 1:656–665

31. Zhang Y, He S, Guo W, Hu Y, Huang J, Mulcahy JR, Wei WD (2018) Surface-plasmon-driven hot electron photochemistry. Chem Rev 118:2927–2954

32. Long J, Chang H, Gu Q, Xu J, Fan L, Wang S, Zhou Y, Wei W, Huang L, Wang X, Liu P, Huang W (2014) Gold-plasmon enhanced solar-to-hydrogen conversion on the {001} facets of anatase TiO_2 nanosheets. Energy Environ Sci 7:973–977

33. Liu Y, Chen P, Chen Y, Lu H, Wang J, Yang Z, Lu Z, Li M, Fang L (2016) In situ ion-exchange synthesis of SnS_2/g-C_3N_4 nanosheets heterojunction for enhancing photocatalytic activity. RSC Adv 6:10802–10809

34. Yang C, Wang W, Shan Z, Huang F (2009) Preparation and photocatalytic activity of high-efficiency visible-light-responsive photocatalyst SnS_x/TiO_2. J Solid State Chem 182:807–812

35. Liu Q, Lu H, Shi Z, Wu F, Guo J, Deng K, Li L (2014) 2D $ZnIn_2S_4$ nanosheet/1D TiO_2 nanorod heterostructure arrays for improved photoelectrochemical water splitting. ACS Appl Mater Inter 6:17200–17207

36. Li X, Yu J, Low J, Fang Y, Xiao J, Chen X (2015) Engineering heterogeneous semiconductors for solar water splitting. J Mater Chem A 3:2485–2534

37. Su T, Shao Q, Qin Z, Guo Z, Wu Z (2018) Role of interfaces in two-dimensional photocatalyst for water splitting. ACS Catal 8:2253–2276

38. Liu S, Li H, Mo R, Chen Q, Yang S, Zhong J (2016) ZnSe sensitized and co-pi catalyzed TiO_2 nanowire array photoanode for solar-driven water splitting. J Electrochem Soc 163:H744–H749

39. Wang L, Liu X, Luo J, Duan X, Crittenden J, Liu C, Zhang S, Pei Y, Zeng Y, Duan X (2017) Active site self-optimization by irreversible phase transition of 1T-MoS_2 in photocatalytic hydrogen evolution. Angew Chem 129:7718–7722

40. Yu J, Xu CY, Ma FX, Hu SP, Zhang YW, Zhen L (2014) Monodisperse SnS_2 nanosheets for high-performance photocatalytic hydrogen generation. ACS Appl Mater Inter 6:22370–22377

41. Fu Y, Cao F, Wu F, Diao Z, Chen J, Shen S, Li L (2018) Phase-modulated band alignment in CdS nanorod/SnS_x nanosheet hierarchical heterojunctions toward efficient water splitting. Adv Funct Mater 28:1706785

42. Huang E, Yao X, Wang W, Wu G, Guan N, Li L (2017) SnS_2 nanoplates with specific facets exposed for enhanced visible-light-driven photocatalysis. ChemPhotoChem 1:60–69

43. Luo B, Liu G, Wang L (2016) Recent advances in 2D materials for photocatalysis. Nanoscale 8:6904–6920

44. Yan X, Ye K, Zhang T, Xue C, Zhang D, Ma C, Wei J, Yang G (2017) Formation of three-dimensionally ordered macroporous TiO_2@nanosheet SnS_2 heterojunctions for exceptional visible-light driven photocatalytic activity. New J Chem 41:8482–8489

45. Christoforidis KC, Sengele A, Keller V, Keller N (2015) Single-step synthesis of SnS_2 nanosheet-decorated TiO_2 anatase nanofibers as efficient photocatalysts for the degradation of gas-phase diethylsulfide. ACS Appl Mater Inter 7:19324–19334

46. Sun X, Yang X, Xiang H, Mi H, Zhang P, Ren X, Li Y, Li X (2019) Nitrogen-doped CoO_x/carbon nanotubes derived by plasma-enhanced atomic layer deposition: efficient bifunctional electrocatalyst for oxygen reduction and evolution reactions. Electrochim Acta 296:964–971

47. Yu J, Zhong Y, Wu X, Sunarso J, Ni M, Zhou W, Shao Z (2018) Bifunctionality from synergy: CoP nanoparticles embedded in amorphous CoO_x nanoplates with heterostructures for highly efficient water electrolysis. Adv Sci 5:1800514

48. Peerakiatkhajohn P, Yun JH, Chen H, Lyu M, Butburee T, Wang L (2016) Stable hematite nanosheet photoanodes for enhanced photoelectrochemical water splitting. Adv Mater 28:6405–6410

49. Yang L, Chu D, Chen Y, Wang W, Zhang Q, Yang J, Zhang M, Cheng Y, Zhu K, Lv J, He G, Sun Z (2016) Photoelectrochemical properties of Ag/TiO_2 electrodes constructed using vertically oriented two-dimensional TiO_2 nanosheet array films. J Electrochem Soc 163:H180–H185

50. Dong Y, He K, Yin L, Zhang A (2007) A facile route to controlled synthesis of Co_3O_4 nanoparticles and their environmental catalytic properties. Nanotechnology 18:435602

51. Gabe A, García-Aguilar J, Berenguer-Murcia Á, Morallón E, Cazorla-Amorós D (2017) Key factors improving oxygen reduction reaction activity in cobalt nanoparticles modified carbon nanotubes. Appl Catal B Environ 217:303–312

52. Tian F, Zhang Y, Zhang J, Pan C (2012) Raman spectroscopy: a new approach to measure the percentage of anatase TiO_2 exposed (001) facets. J Phys Chem C 116:7515–7519

53. Tu F, Xu X, Wang P, Si L, Zhou X, Bao J (2017) A few-layer SnS_2/reduced graphene oxide sandwich hybrid for efficient sodium storage. J Phys Chem C 121:3261–3269

54. Yang L, Zhang Q, Wang W, Ma S, Zhang M, Lv J, He G, Sun Z (2016) Tuning the photoelectronic and photocatalytic properties of single-crystalline TiO_2 nanosheet array films with dominant {001} facets by controlling the hydrochloric acid concentration. J Mater Sci 51:950–957

55. Zhuang HL, Hennig RG (2013) Theoretical perspective of photocatalytic properties of single-layer SnS_2. Phys Rev B 88:115314

56. Johny J, Sepulveda Guzman S, Krishnan B, Avellaneda Avellaneda D, Shaji S (2018) Nanostructured SnS_2 thin films from laser ablated nanocolloids: structure, morphology, optoelectronic and electrochemical properties. ChemPhysChem 19:2902–2914

57. Fu CF, Wu X, Yang J (2018) Material design for photocatalytic water splitting from a theoretical perspective. Adv Mater 30:1802106

58. Chen H, Lyu M, Zhang M, Feron K, Searles DJ, Dargusch M, Yao X, Wang L (2017) Switched photocurrent on tin sulfide-based nanoplate photoelectrodes. ChemSusChem 10:670–674

59. Zhang Z, Huang J, Zhang M, Yuan Q, Dong B (2015) Ultrathin hexagonal SnS_2 nanosheets coupled with g-C_3N_4 nanosheets as 2D/2D heterojunction photocatalysts toward high photocatalytic activity. Appl Catal B Environ 163:298–305

60. Wu Z, Xue Y, Zhang Y, Li J, Chen T (2015) SnS_2 nanosheet-based microstructures with high adsorption capabilities and visible light photocatalytic activities. RSC Adv 5:24640–24648

Publisher's Note